MECHANISMS OF MINING INDUCED INRUSH OF PRESSURIZED WATER IN THE FLOOR CONTAINING FAULTS

BAOLIANG ZHANG, WEI ZHANG

School of Architecture and Engineering, Liaocheng University, Liaocheng, China

corresponding author Wei Zhang, e-mail: 1125671372@qq.com

BAOTANG SHEN

The Commonwealth Scientific and Industrial Research Organisation, Queensland, Australia

YANG GAO

School of Architecture and Engineering, Liaocheng University, Liaocheng, China

MINGMING LIU

Water-Sediment Regulation and Sand Effective Utilization Special Laboratory of Shandong Provincial Education Department, Liaocheng University, Liaocheng, China

Investigating the propagation of the seepage path of confined water in the floor is an important means to determine the conditions of water inrush from the mine floor for deep mines with high water pressure. In order to better understand the mechanisms of water inrush due to the hidden fault floor above a confined water body, an integrated study including analytical analysis, and similarity simulation experiments were conducted. The study focuses on the distribution of mining induced stress in the floor, the propagation of hidden faults, and the evolution process of water inrush channels during longwall coal seam extraction.

Keywords: floor concealed fault, water inrush mechanism, mining-water pressure action, crack propagation, seepage path

1. Introduction

Mine water inrush has always been a prominent problem that threatens safety of coal production. In recent years, most coal mines in northern China are gradually entering deep mining. The distance between the main coal seam and the aquifer of the lower Ordovician limestone formation is shrinking, and the threat of floor water inrush is becoming increasingly serious (Yin *et al.*, 2021; Zhang *et al.*, 2023a; Cao *et al.*, 2021). Among them, the Han-Xing mining area is one of the typical mining areas with high water inflow in China (Pappalardo *et al.*, 2020). The coal seam is overlaying an Ordovician limestone karst layer with water pressure of over 7.0 MPa, and over 10 large-scale water inrush incidents occurred in the past 20 years, of which 9 occurred in the mining face. Under the disturbance of deep mining and high water pressure, the mining is facing serious water inrush threats. The presence of small hidden faults in the floor further exacerbates the risk of water inrush (Zhao *et al.*, 2018; Zhang *et al.*, 2020a,b,c; Mezza *et al.*, 2022).

The water inrush caused by floor aquifers must have a water inrush path, and formation mechanisms of the water inrush path are the key to control and remediate the water inrush risk. The concealed fault is a natural path for the migration of confined water, which has a profound impact on the stress state of floor and rock permeability, and will significantly increase the original height of water migration (Aguilera *et al.*, 2019; Bhuiyan *et al.*, 2018; Zhang *et al.*, 2020a,b,c). Under specific mining geological conditions, the surrounding rock undergoes periodic

caving with the movement of the working face. Due to the propagation of primary fractures in hidden faults and low mechanical strength, the integrity of water barrier in the floor rock layer is weakened to various degrees. The impact of mining and the propagation of mining fractures in the floor region vary depending on the structural geological conditions (Guerin *et al.*, 2021; Lin *et al.*, 2021). Li *et al.* (2023) established a solid fluid coupling mathematical model and analyzed the relationship between fault elements and water inrush law by using finite element simulation. Yin *et al.* (2022) developed a mechanical model for progressive uplift of faults and derived an analytical formula for the critical mechanics of water inrush from faults, revealing the spatiotemporal evolution of water inrush from the floor through physical simulation. Based on theoretical analysis and numerical simulation, Ren *et al.* (2022) conducted an in-depth study on the characteristics of mining induced floor fault activation and delayed water inrush, and obtained the mechanism of induced fault activation and delayed water inrush under the influence of mining.

Despite the increasing awareness and importance of mine water inrush, floor water inrush accidents still occur from time to time. Based on the investigation and statistics of the causes of multiple large-scale water inrush accidents, Wang *et al.* (2022) pointed out that the reason for the difficulty in containing water inrush accidents in the floor is the concealment and difficulty in detecting hidden small structures. Based on this, the traditional method of preventing and controlling mine water in coal mining faces has been changed, and a regional approach tailored to the mining area has been adopted. The location and scale of hidden structures are determined by injecting a grout slurry and observe its leakage. The method of microseismic monitoring and warning for mine water hazards is adopted by Xiong *et al.* (2023), which describes and predicts the trajectory of water inrush by monitoring the microseismic signals generated during the formation and dynamic development of potential water conducting cracks. The tri-level warning model for mine water inrush established from this can help managing potential water inrush areas, providing a new method for deep hidden structure exploration, dynamic monitoring, and water inrush warning. For the study of the mechanism of coal seam floor damage and water inrush, Tu *et al.* (2022) proposed the concept of "relative water resistance layer of the floor", pointing out that water inrush from the coal seam floor is not only related to thickness of the water resistance layer, but also to water pressure. By analyzing a large amount of on-site measured data, Zhang *et al.* (2020a,b,c) considered the joint control effect of mining stresses and water pressure in the floor rock mass, and proposed the in-situ tensile fracture theory. In view of the spatial relationship between the water conducting fault and the floor plastic slip zone, the shortest distance between the water conducting fault and the floor plastic slip zone is regarded as the critical path of the fault water inrush, and a simplified fracture mechanics model of the floor fault water inrush is established by Zhao *et al.* (2020). Based on the theory of linear elasticity stress propagation in a semi infinite body, the confined water pressure is regarded as an additional stress, and the distribution law of mining induced stress in the floor is obtained by Zhang *et al.* (2022a,b,c), which is used as the basis for judging the risk of water inrush. Based on the stress calculation results of the floor, the Mohr-Coulomb criterion with tensile failure was used to calculate the depth of the floor plate failure, and the effects of water pressure and thickness of the waterproof floor plate on the calculation results were explored by Mineo and Pappalardo (2019).

The present research focuses on the activation of hidden faults and the mechanism of water inrush under the combined action of mining and water pressure. The propagation direction of the seepage path of pressurized water after mining is crucial for determining the scope of key regional governance objectives (Zhang *et al.*, 2022a,bc; Zhang *et al.*, 2023a,b). The water inrush from the coal seam floor is caused by mining disturbances that cause stress field changes, leading to the initiation and propagation of cracks in the floor. Under the impact of high pressure water from the bottom to top, the seepage path gradually evolves into a high-speed water inrush path.

The distribution characteristics of stress field, crack propagation, and seepage behavior of the floor will also vary depending on whether the floor contains hidden structures and the types of hidden structures. Therefore, it is still necessary to further analyze the linkage process between the uplift and migration of mining induced confined water and the development of water path under the combined conditions. This paper adopts an integrated approach combining theoretical analysis, physical simulation, and numerical simulations under the conditions of the existence of hidden faults in the floor. The water inrush mode of hidden faults in the floor is the key research object of this study, and the process of water inrush caused by mining through hidden faults is analyzed to study the mechanism of floor water inrush in deep mining.

2. Simulation experiment on the expansion and activation of hidden faults

2.1. Determination of similarity ratio

The expansion of hidden faults refers to the process of relative opening displacement of the rock layers of the fault under the combined action of external stress and floor support pressure, with the direction of relative displacement determined by the maximum stress direction. Essentially, it is the shear and expansion movement that occurs in the sidewalls of the fault failure zone under the action of mining pressure, causing the material position inside the fault to change from the initial non hydraulic state to a hydraulic state.

The two key factors that can affect water inrush from the floor while maintaining the same hydrological conditions are the mining stress and faults (including size and spatial location). They reduce the effective thickness of the floor waterproof layer. As shown in Fig. 1, water inrush from hidden faults in the coal seam floor is the main form of water inrush from faults. Therefore, the hidden faults in the floor are taken as the main analysis object. When the inclination angle of the hidden faults is α, as the coal seam is mined, if the support pressure on the floor is greater than the maximum deformation strength value, plastic deformation will occur in the rock mass within a certain range of the working face floor, leading to the phenomenon of floor protrusion. The depth of the impact of mining stress on the failure of the bottom plate is L.
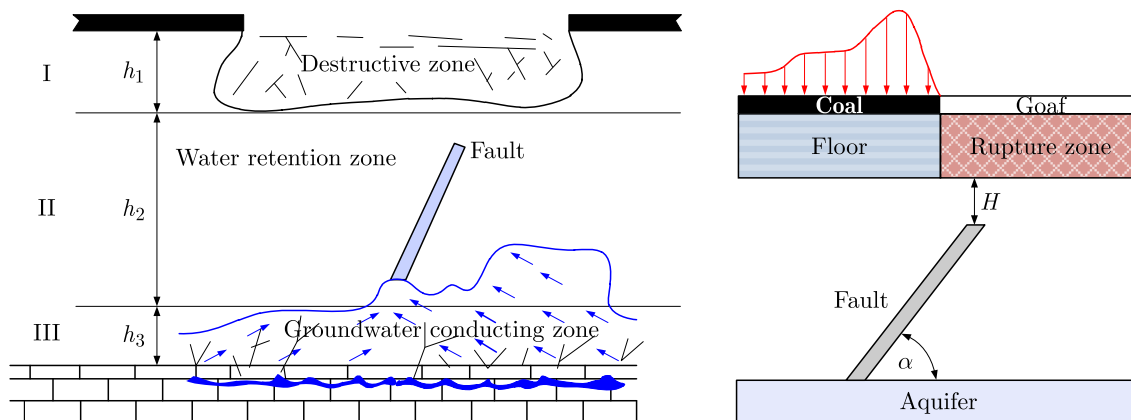

Fig. 1. Structural model of water inrush from floor faults

It is necessary to conduct relevant physical similarity simulation tests to address the above issues. Figure 2 shows the plane stress similarity simulation test independently developed and designed. The bracket has height of 1.5 m, width of 2 m, and thickness of 0.2 m. During the testing process, strain information was collected through the DH3821 static strain analyzer, and stress information was obtained based on the LY-350 soil pressure sensor.

Fig. 2. Schematic diagram of the testing device: (a) test bracket, (b) strain analyzer, (c) pressure cell

The similarity simulation test is based on mining technical conditions, combined with geometric dimensions of the support and based on similarity theory, to determine the simulation similarity ratio:

— geometric similarity ratio

$$C_1 = \frac{x'}{x''} = \frac{y'}{y''} = 100 \tag{2.1}$$

— unit weight similarity ratio

$$C_\gamma = \frac{\gamma'}{\gamma''} = 1.5 \tag{2.2}$$

— time similarity ratio

$$C_\tau = \sqrt{C_1} = 14.1 \tag{2.3}$$

— strength similarity ratio

$$C_p = C_e = C\gamma C_1 \tag{2.4}$$

2.2. Design of the compensated stress measuring point layout

Taking into account the size of the support and the objective impact of boundary coal pillars on the test results, a 20 cm boundary coal pillar is left on both sides of the model. The working face is pushed from left to right, with total length of 150 cm. The model design simulation adopts a long wall full height mining method, and the simulated working face completes mining every 30 min, with parallel operations.

As shown in Fig. 3, due to the height limitation of the test bench, when studying the movement law of the overlying strata in deep mining through experiments, it is not possible to simulate all rock layers. Only a portion of the overlying strata in the mining space can be simulated, and the weight of the remaining overlying strata and the topsoil layer needs to be simplified as a uniformly distributed load applied to the upper boundary of the model. Removing the thickness of the floor, as the actual height of the model laid is 1.09 m, removing the thickness of the floor, calculated in a similarity ratio of 1:100, is equivalent to simulating a 690 m high overburden layer. For a working face with an average mining depth of 1000 m, the remaining 310 m of overlying rock and quaternary clay are simplified as surface loads applied to the top of the model. The vertical stress that the model needs to compensate for can be calculated using the following expression

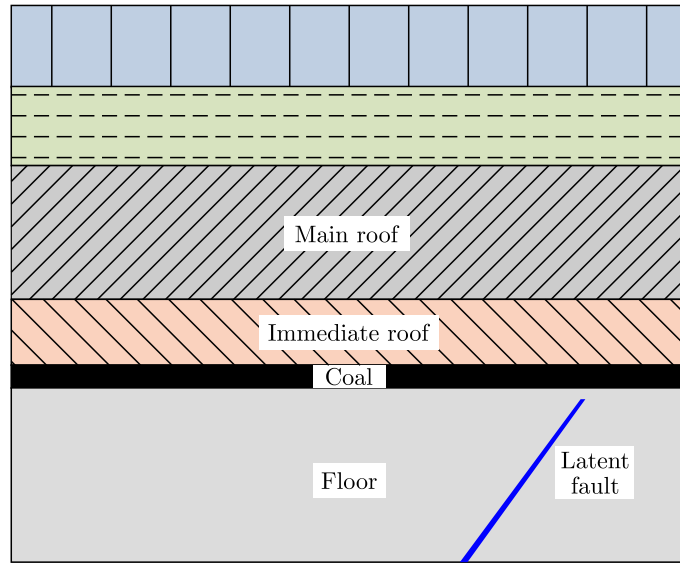$$\sigma'' = \frac{C'}{C_p} = \frac{\gamma H}{C_p} \tag{2.5}$$

Fig. 3. Similar simulation structural model

2.3. Measuring point layout

As shown in Fig. 4, a total of 10 stress sensors are used in the similar material model to monitor the stress characteristics of the roof and floor in the coal seam during excavation. Among
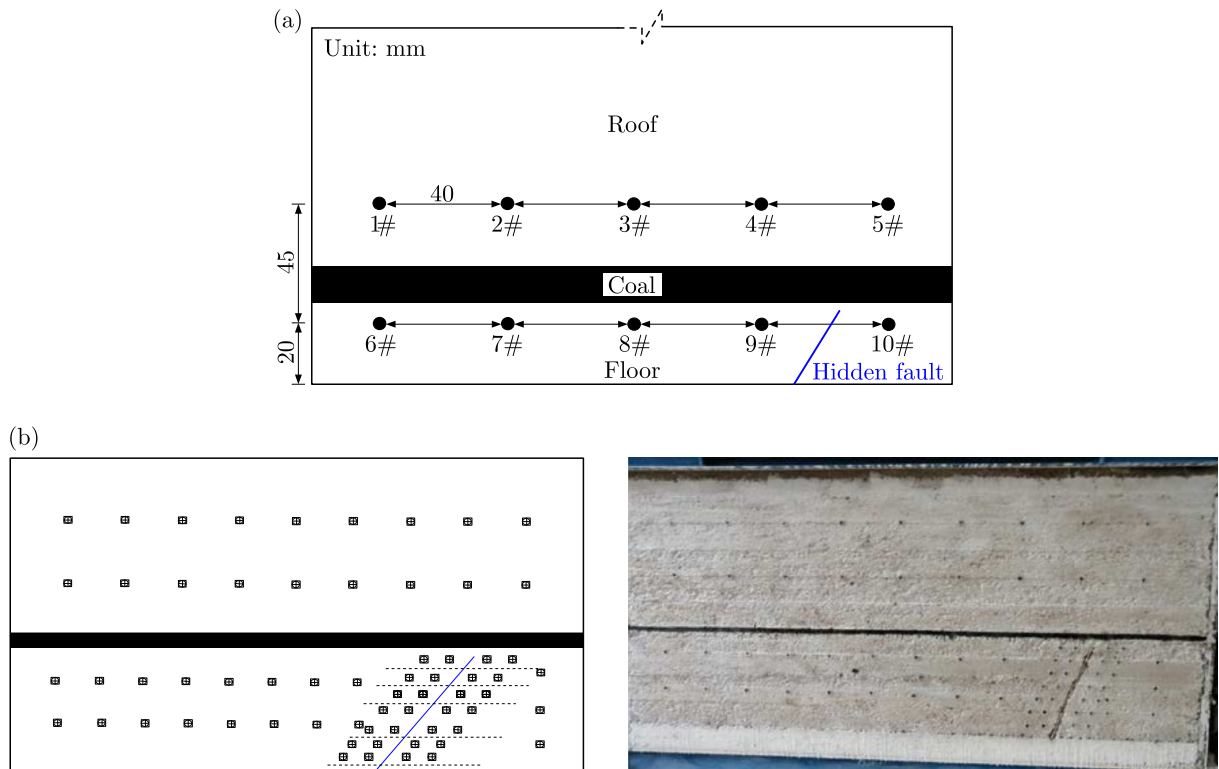

Fig. 4. Schematic diagram of measurement point layout location: (a) of stress gauge layout position, (b) layout of strain gauge

them, the first group has five strain gauges which are uniformly arranged in the medium grained sandstone of the 15th layer of the coal seam roof. The second group consists of five strain gauges which are uniformly arranged in the 19th layer of siltstone. In addition, there are a total of 66

displacement monitoring points for similar material models, and they are arranged in 4 areas. Among them, the distance between the horizontal and vertical displacement monitoring points in the roof is 20 cm. The distance between the horizontal and vertical displacement monitoring points in the left floor of the fault is 15 cm. The vertical distance interval between the monitoring points on the right side of the fault floor is 10 cm. The distance between the displacement monitoring points near the hidden fault and the fault, as well as the horizontal and vertical distances between the two monitoring points are 5 cm.

2.4. Similar material model laying

By combining hydrogeological conditions with experimental methods, a similar material model simulates a 69 m thick roof, a 2 m thick coal seam, and a 38 m thick floor. According to the model parameters and similarity ratio given in Table 1, sand, calcium carbonate, gypsum, and water are used to make the test materials. After the materials are mixed and stirred evenly, they are laid layer by layer. After each layer of rock is laid, mica powder needs to be spread to simulate the layer of the rock, and the laying is carried out step by step until the entire model laying work is completed.

Table 1. Stratification and ratio of rock layers

No.	Lithology	Thickness of stratum [cm]	Accumulated thickness [cm]	Proportion ratio	Coal material usage [kg]			
					sand	calcium carbonate	gypsum	water
1	Sandstone	3	3	7:8:2	19.4	1.7	0.4	2.2
2	Siltstone	10	13	7:5:5	67.2	4.8	4.8	7.7
3	Sandstone	5	18	7:8:2	33.6	3.8	1.0	3.8
4	Mudstone	6	24	9:6:4	37.8	3.2	2.2	4.3
5	Sandstone	10	34	7:7:3	69.1	1.2	6.5	7.7
6	Siltstone	8	42	7:5:5	27.6	1.5	1.5	3.1
7	Sandstone	2	44	7:8:2	12.6	1.4	0.4	1.4
8	Siltstone	2	46	7:5:5	13.4	1.0	1.0	1.5
9	Sandstone	6	52	7:7:3	41.5	3.2	1.3	4.6
10	Mudstone	2	54	9:6:4	13.0	0.9	0.6	1.4
11	Sandstone	2	56	7:8:2	13.8	1.2	0.3	1.5
12	Siltstone	4	60	7:5:5	27.5	1.5	1.5	3.1
13	Sandstone	2	62	7:8:2	13.0	1.2	0.3	1.4
14	Siltstone	1	63	7:5:5	6.9	0.4	0.4	0.8
15	Sandstone	5	68	7:7:3	33.6	3.4	1.4	3.8
16	Mudstone	1	69	9:6:4	6.5	0.4	0.3	0.7
17	Coal	2	71	8:6:4	9.5	0.6	0.4	1.1
18	Mudstone	3	74	9:6:4	18.9	1.6	1.1	2.2
19	Siltstone	5	79	8:6:4	33.6	2.9	1.9	3.8
20	Sandstone	12	91	7:7:3	80.6	8.1	3.5	9.2
21	Mudstone	2	93	9:6:4	13.0	0.9	0.6	1.4
22	Siltstone	1	94	7:5:5	6.7	0.5	0.5	0.8
23	Sandstone	15	109	7:8:2	100.8	11.5	2.9	11.5

As shown in Fig. 5, the laying steps of a similar material simulation model are:

(1) In the early stage, the required quality of each material is calculated in advance based on the size and proportion of the test frame for on-site weighing, the grade of sand and high-

-strength gypsum is determined, and the required frame for the test is checked to ensure its normal use and compliance with performance requirements.

(2) Weigh the material according to the calculated ratio, and when weighing the material, it is necessary to weigh the excess mass. In actual experiments, there may be a decrease in the total amount of the material due to operational reasons (such as material sticking to the mixer, scattering during transportation, etc.), so it is necessary to weigh according to the excess mass.

(3) According to the experimental needs, the template for simulating faults should be placed in advance. Stress sensors should be placed in the rock layers designed for the model, and placed according to the predesigned positions. The stress gauge labels at each position should be recorded to facilitate data processing in the future without confusion.

(4) Weigh each material according to the precalculated material quality and lay it from the bottom to top according to the layer size. During the laying process, sufficient compaction is required to ensure that there will be no significant settlement during the later static process, thereby ensuring the accuracy of the test results.

(5) Spread mica powder between each rock layer (simulating the layered rock layer). After the overall laying is completed, only external loads are applied based on the precalculated loads to simulate the overlying rock that cannot be reflected in the upper part. Place the model for 3 days and maintain it in a room temperature curing state.

Fig. 5. Laying process of a similar material model

3. Analysis of test results

3.1. Analysis of the characteristics of layer deformation

Considering the impact of boundary effects on coal seam mining, the initial mining position is set at a distance of 20 cm from the support boundary. Each excavation distance is 5 cm, the excavation height is 2 cm, and the excavation interval is 30 minutes. In addition, the local and global deformation characteristics of similar material models at intervals of 10 minutes are recorded.

During the entire testing process, a total of 32 excavations were conducted, with total excavation length of 160 cm. As the mining progress increases, the impact of mining stress generated by this disturbance on the roof gradually increases. After the appearance of the initial pressure characteristics, the width and height of fault cracks undergo varying degrees of evolution. A total of 13 push mining cases that met the periodic weighing characteristics were statistically analyzed throughout the entire experiment process. Among them, when the initial pressure is applied at 25 cm during mining, cracks appear on the direct roof, and fracture occurs when the collapse step is reached, with a fracture step of about 25 m (Fig. 6).

As shown in Fig. 7, the curve evolution characteristics illustrate the lateral displacement characteristics of the observation points set on both sides of the fault crack after each compression. When the value in the figure is positive, it indicates that the fault is expanding outward and the failure mode is tensile failure. When the value in the figure is negative, it indicates that
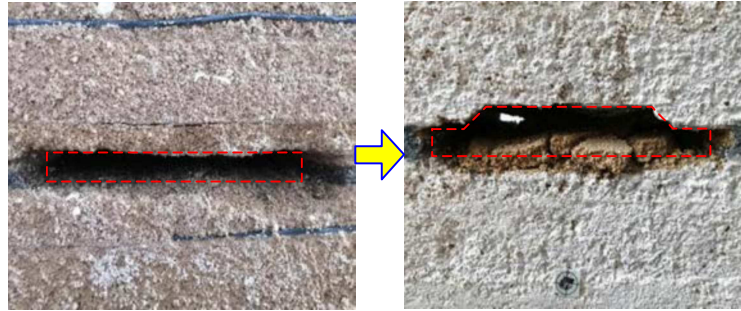
Fig. 6. Initial pressure on the working face

the fault is contracting inward and the failure mode is compression failure. During the testing process, the fault cracks showed overall compression failure, and compression deformation in the middle of the fault was the largest. The X distribution characteristics of deformation on both sides of the fault indicate that the middle part of the fault is in a compression and contraction state, while the two ends of the fault are in an expansion state. After the third pressure application during the experiment, there was no lateral displacement at the bottom of the fault until it continued to grow after the sixth pressure application, indicating that the crack propagation was a process from closure to opening.
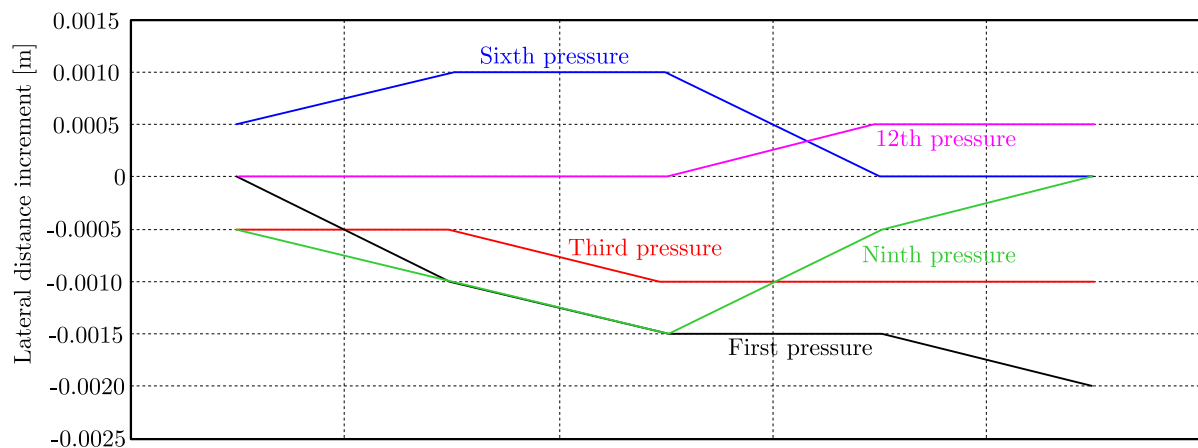

Fig. 7. Characteristics of lateral displacement changes on both sides of faults

When the working face advances 50 cm, the indirect roof collapses. When the working face is advanced to 60 cm, the crack extends to the top plate at 52 cm. When the working face was advanced to 95 cm, the crack had expanded to 67 cm. When the working face is advanced to 140 cm, the crack extends to 109 cm and runs through a similar material model (Fig. 8).

3.2. Analysis of stress evolution characteristics

Sensors 1 and 10 are symmetrically distributed in the direct roof, and are located behind the cutting hole and in front of the stop mining line. As shown in Fig. 9, by comparing and analyzing the distribution characteristics of support stress in the direct roof of the coal wall side, it is found that during the advancing process of the working face, the support stress has always been in an upward state and can be divided into two stages: a slow increase and a rapid increase. It indicates that during the mining process, the overlying rock at the opening has been constantly moving and deformed. During the process of advancing to a distance of 95 cm from the opening off cut, the supporting stress rises slowly. After the working face is advanced to 95 cm, the support stress begins to rapidly increase. When the working face is 60 cm away from
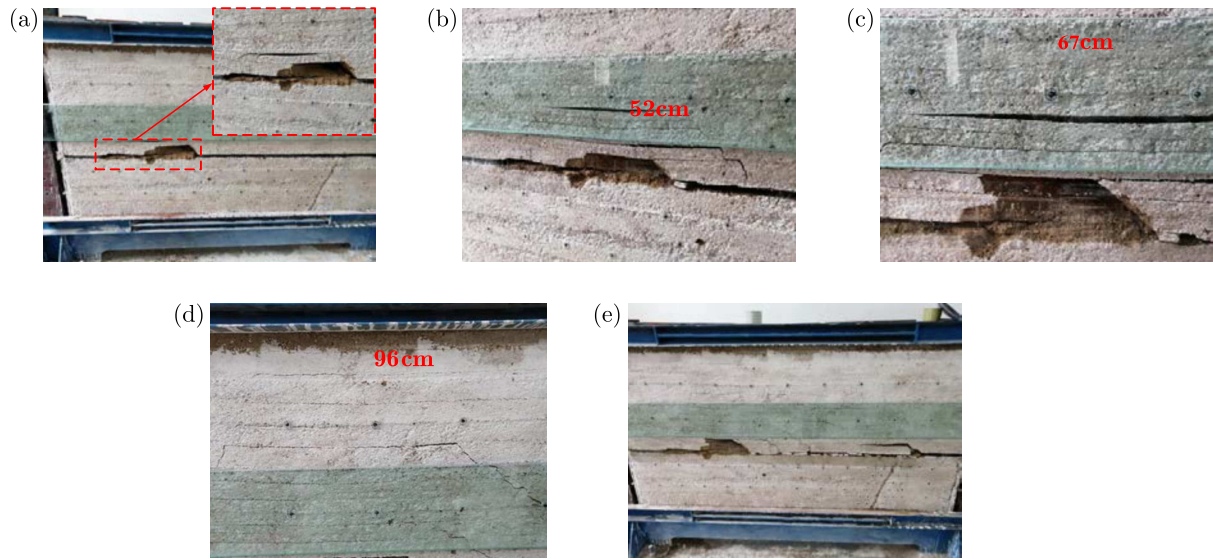
Fig. 8. Deformation characteristics of similar material models: (a) indirect roof collapse, (b) roof crack length is 52 cm, (c) roof crack length is 67 cm, (d) roof crack length is 96 cm, (e) final structure of the model
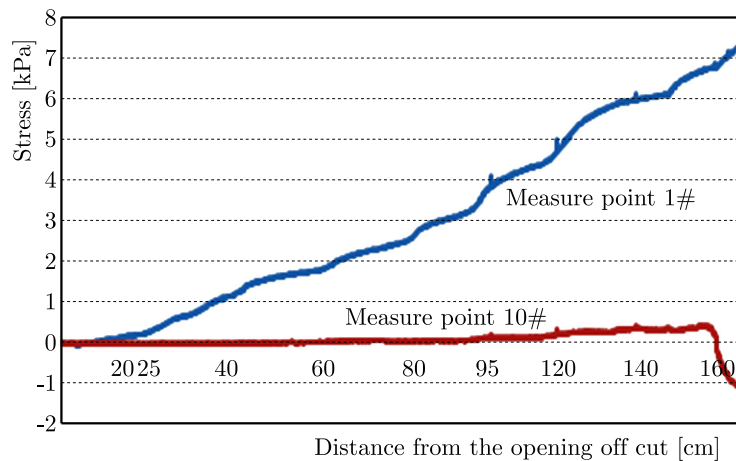

Fig. 9. Stress distribution characteristics of the direct top support

the stopping line, the growth rate of bearing stress decreases. When the working face is 20 cm away from the stopping line, the support stress rapidly decreases. In the process of deep mining, the impact range of mining is relatively large, and within 20 m from the coal wall of the working face, there is a stress rise zone. Moreover, the movement and deformation of the overlying strata at the opening are more severe than at the stopping line.

In the pushing mining process of the working face, the bearing stress in the immediate roof and floor in front of the coal wall experienced a process of rising first and then falling. Due to the large range of advanced influence, the support stress in the top and bottom plates in front of the working face gradually increases, with the maximum value of the top plate support stress being about 5 kPa and the maximum value of the bottom plate support stress being about 8 kPa. After the working face is pushed and mined, the support stress will rapidly decrease. When the distance between the mining line and the goaf is about 30 cm 40 cm, the increment of support stress tends to stabilize, and the final stress values are inconsistent with the position in the goaf. In addition, the stress in the bottom plate gradually changes from a positive value to a negative value, indicating that the bottom plate has undergone a process from compression to expansion (Fig. 10).
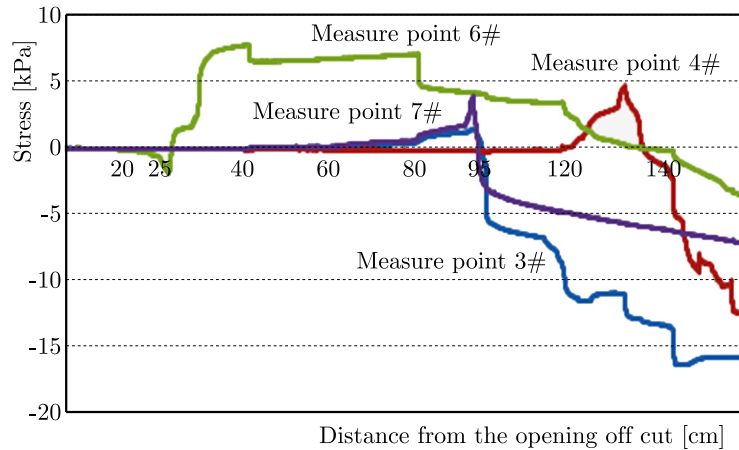
Fig. 10. Distribution characteristics of support stress in the goaf

The maximum decrease in stress increment at the center of the mining area indicates that the place with the maximum deformation caused by the direct roof movement is located near the center of the mining area. The increment of basic top stress shows a trend of first decreasing and then increasing during the process of pushing and mining 35 cm to 40 cm in the working face, indicating that the separation layer between the direct top and the upper rock layer is gradually compacted and closed, so a part of the weight of the upper rock layer is borne by the direct top. After the completion of the working face push mining, the stress increment value of the direct roof in the goaf is basically zero, indicating that the movement and deformation of the direct roof rock in the goaf have become stable. The stress of the floor shows a trend of a rapid increase first and then a slow decrease. The stress of the bottom plate increases with a decrease of the distance from the working face pushing and mining line, and undergoes an evolution process of compression before expansion.
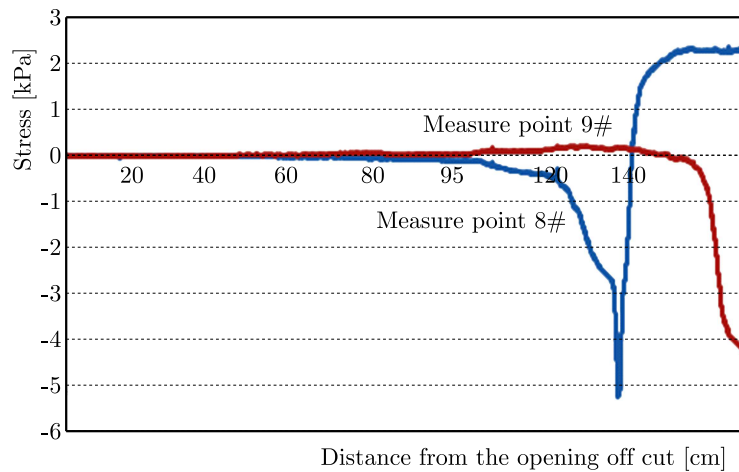

Fig. 11. Characteristics of stress distribution in the fault

The impact of early mining on the stress at the fault is very small, so the stress on both sides of the fault changes slowly, and the overall trend shows a slow increase followed by a rapid decrease. Before the working face is advanced to a distance of 25 cm above the fault, the stress at the fault is basically positive, and then the fault stress rapidly decreases and transforms into a negative value. When the working face is pushed to a distance of 25 cm from the fault, the left side of the fault is pulled and the right side is compressed, and the fault has a tendency to rupture to the upper left. When the working face is pushed to be within 25 cm from the fault,

the left side of the fault is under pressure and the right side is under tension, with a tendency to rupture above the right (Fig. 11).

4. Conclusion

- Under the influence of mining, the edge of macroscopic hidden faults is mainly characterized by oblique shear failure accompanied by overall splitting tensile failure. The shear cracks derived from edge cracks and oblique cracks develop in opposite directions, and the development direction is the shortest path direction required for crack penetration.
- The rock mass near the hidden fault has undergone an evolutionary process of "development of the original separation layer, compaction and sealing of the original separation layer, expansion of the new separation layer, and compaction and sealing of the new separation layer". When the working face advances to a height near three times the fault height, the impact of mining stress on the development of the fault sharply increases.
- When a distance from the working face is greater than 10 times the height of the fault, the vertical stress of the surrounding rock near the macroscopic hidden fault is basically not affected by the mining stress. When the distance from the working face is less than 5 times the height of the fault, the vertical stress of the surrounding rock near the macroscopic hidden fault is gradually affected by the mining stress.

References

1. Aguilera M.A., Arias R.M., Manzur T., 2019, Mapping microhabitat thermal patterns in artificial breakwaters: Alteration of intertidal biodiversity by higher rock temperature, Ecology and Evolution, **9**, 22, 12915-12927

2. Bhuiyan M.Y., Lin B., Giurgiutiu V., 2018, Acoustic emission sensor effect and waveform evolution during fatigue crack growth in thin metallic plate, *Journal of Intelligent Material Systems and Structures*, **29**, 7, 1275-1284

3. Cao K.W., Ma L.Q., Wu Y., Khan N.M., Spearing A.J.S., Hussain S., Yang J., 2021, Cyclic fatigue characteristics of rock failure using infrared radiation as precursor to violent failure: Experimental insights from loading and unloading response, *Fatigue and Fracture of Engineering Materials and Structures*, **44**, 2, 584-594

4. Guerin A., Jaboyedoff M., Collins B. D., Stock G. M., Derron M. H., Abellan A., Matasci B., 2021, Remote thermal detection of exfoliation sheet deformation, *Landslides*, **18**, 3, 865-879

5. Li G., Zhu C., He M.C., Zuo Y.J., Gong F.Q., Xue Y.G., Feng G.L., 2023, Intelligent method for parameters optimization of cable in soft rock tunnel base on longitudinal wave velocity, *Tunnelling and Underground Space Technology incorporating Trenchless Technology Research*, **133**, 104905

6. Lin Q.B., Cao P., Liu Y.Z., Cao R.H., Li J.T., 2021, Mechanical behaviour of a jointed rock mass with a circular hole under compression-shear loading: Experimental and numerical studies, *Theoretical and Applied Fracture Mechanics*, **114**, 102998

7. Mezza S., Vazquez P., Ben M'barek Jemai M., Fronteau G., 2022, Infrared thermography for the investigation of physical-chemical properties and thermal durability of Tunisian limestone rocks, *Construction and Building Materials*, **339**, 127470

8. Mineo S., Pappalardo G., 2019, InfraRed Thermography presented as an innovative and non-destructive solution to quantify rock porosity in laboratory, *International Journal of Rock Mechanics and Mining Sciences*, **115**, 99-110

9. Pappalardo G., Mineo S., Imposa S., Grassi S., Leotta A., Rosa F.L., Salerno D., 2020, A quick combined approach for the characterization of a cliff during a post-rockfall emergency, *Landslides*, **17**, 5, 1063-1081

10. Ren F.Q., Zhu C., He M.C., Shang J.L., Feng G.L., Bai J.W., 2022, Characteristics and precursor of static and dynamic triggered rockburst: Insight from multifractal, *Rock Mechanics and Rock Engineering*, **56**, 3, 1945-1967

11. Tu W.F., Li L.P., Zhou Z.Q., Shang C.S., 2022, Thickness calculation of accumulative damaged zone by rock mass blasting based on Hoek-Brown failure criterion, *International Journal of Geomechanics*, **22**, 2, 04021273

12. Wang Q., Xu S., Xin Z.X., He M.C., Wei H.Y., Jiang B., 2022, Mechanical properties and field application of constant resistance energy-absorbing anchor cable, *Tunnelling and Underground Space Technology incorporating Trenchless Technology Research*, **125**, 104526

13. Xiong F., Zhu C., Feng G., Zheng J., Sun H., 2023, A three-dimensional coupled thermo-hydro model for geothermal development in discrete fracture networks of hot dry rock reservoirs, *Gondwana Research*, **122**, 331-347

14. Yin Q., Wu J.Y., Jiang Z., Zhu C., Su H.J., Jing H.W., Gu X.W., 2022, Investigating the effect of water quenching cycles on mechanical behaviors for granites after conventional triaxial compression, *Geomechanics and Geophysics for Geo-Energy and Geo-Resources*, **8**, 2, 77

15. Yin Q., Wu J.Y., Zhu C., He M.C., Meng Q.X., Jing H.W., 2021, Shear mechanical responses of sandstone exposed to high temperature under constant normal stiffness boundary conditions, *Geomechanics and Geophysics for Geo-Energy and Geo-Resources*, **7**, 2, 1-17

16. Zhang C.Q., Cui G.J., Deng L., Zhou H., Lu J.J., Dai F., 2020a, Laboratory investigation on shear behaviors of bolt-grout interface subjected to constant normal stiffness, *Rock Mechanics and Rock Engineering*, **53**, 3, 1333-1347

17. Zhang C.W., Jin Z.X., Feng G.R., Song X.M., Gao R., Zhang Y.J., 2020b, Double peaked stress-strain behavior and progressive failure mechanism of encased coal pillars under uniaxial compression, *Rock Mechanics and Rock Engineering*, **53**, 7, 3253-3266

18. Zhang X.P., Lv G.G., Liu Q.S., Wu S.C., Zhang Q., Ji P.Q., Tang X.H., 2020c, Identifying accurate crack initiation and propagation thresholds in siliceous siltstone and limestone, *Rock Mechanics and Rock Engineering*, **54**, 2, 973-978

19. Zhang W., Guo W.Y., Wang Z.Q., 2022a, Influence of lateral pressure on mechanical behavior of different rock types under biaxial compression, *Journal of Central South University*, **29**, 11, 3695-3705

20. Zhang W., Xing M.L., Guo W.Y., 2023a, Study on fracture characteristics of anchored sandstone with precast crack based on double K criterion, *International Journal of Solids and Structures*, **275**, 112296

21. Zhang W., Zhao T.B., Guo W.Y., Xing M.L., 2022b, Study on mechanical characteristics of rock type I fracture and anchorage strengthening mechanism, *Journal of Theoretical and Applied Mechanics*, **60**, 3, 423-434

22. Zhang W., Zhao T.B., Yin Y.C., 2022c, Prefabricated fractured rock under stepwise loading and unloading, *Journal of Theoretical and Applied Mechanics*, **60**, 1, 167-179

23. Zhang W., Zhang B.L., Zhao T.B., 2023b, Study on the law of failure acoustic-thermal signal of weakly cemented fractured rock with different dip angles, *Rock Mechanics and Rock Engineering*, **56**, 6, 4557-4568

24. ZHAO T.B., GUO W.Y., TAN Y.L., YIN Y.C., CAI L.S., PAN J.F., 2018, Case studies of rock bursts under complicated geological conditions during multi-seam mining at a depth of 800 m, *Rock Mechanics and Rock Engineering*, **51**, 5, 1539-1564

25. ZHAO T.B., ZHANG W., GU S.T., LV Y.W., LI Z.H., 2020, Study on fracture mechanics of granite based on digital speckle correlation method, *International Journal of Solids and Structures*, **193**, 192-199